

## Research Paper

# Thermal performance and visualization of dual-diameter channel pulsating heat pipes additively manufactured through stereolithography

Md. Jubayer Hossain, Max Pawlick , Bhavin Yardi, Satish Kumar\*

The G.W. Woodruff School of Mechanical Engineering, Georgia Institute of Technology, Atlanta, GA 30332, USA

## ARTICLE INFO

**Keywords:**

Pulsating heat pipe (PHP)  
Dual-diameter channel  
Additive manufacturing (AM)  
Orientation independent  
High-temperature resin

## ABSTRACT

As two-phase passive heat transfer devices, pulsating heat pipes (PHPs) have attracted widespread research interest for their potential to enhance heat dissipation and contribute to energy-efficient thermal management. This study experimentally assesses the thermal behavior and flow-characteristics of PHPs fabricated using Stereolithography (SLA) additive manufacturing technology. The investigation focuses on PHPs with dual-diameter channels, also called non-uniform channels, in three configurations: 2-turn center-heated, 10-turn center-heated, and 10-turn end-heated. Experiments were performed in vertical and horizontal orientations using acetone, except in one test with deionized (DI) water for performance comparison. For baseline comparison, tests were also conducted on uncharged PHPs. Results reveal that 2-turn PHP failed to initiate startup in the horizontal orientation, while all 10-turn PHPs started successfully, emphasizing the importance of increasing turns, even with a capillary-enhanced dual-diameter channel. The 10-turn center-heated PHP demonstrated orientation-independent operation with the lowest thermal resistance of  $\sim 4.7$  K/W, slightly outperforming end-heated cases. With DI water, the 10-turn PHP reached  $121^{\circ}\text{C}$  evaporator temperature at 38.5 W. Flow visualization was conducted to capture fluid movement throughout the PHP channels for 10-turn PHPs in both orientations, revealing differences in flow stability, oscillation amplitude, and liquid distribution, particularly emphasizing the influence of initial fluid distribution on startup in vertical orientations. Evaluation of effective thermal conductivity indicates conventional methods overestimate it for polymer-PHPs by disregarding axial-conduction through heat sources and sinks. A refined methodology is proposed for improved accuracy. These insights pave the path for optimizing polymer-based PHPs for thermal management applications requiring low-mass, low-cost, or electrically insulating solutions.

## 1. Introduction

As electronic devices become more powerful and compact, effective thermal management is crucial for ensuring that systems and components operate within safe temperature ranges, reducing the risk of damage and failure. The growing focus on climate change has led to an increased demand for energy-efficient thermal management methods that can minimize environmental impact and lower operational costs [1]. This demand aligns closely with advancements in semiconductor technology, where improvements in device performance often come at the expense of increased heat generation. Consequently, enhancing the performance of thermal management systems has become imperative to maintain the junction temperature of electronic devices below critical thresholds, ensuring optimal functionality and longevity [2]. As the industry continues to push the boundaries of device capabilities,

innovative cooling solutions are becoming increasingly vital to overcome the thermal barriers that threaten to impede technological advancement. For many applications, especially with low heat fluxes, the passive thermal management solutions become very attractive.

Researchers have explored various heat dissipation technologies tailored for electronic applications. One of the most widely adopted passive thermal management solutions is the heat pipe, a highly efficient and compact design that has become a cornerstone of electronic cooling systems. However, conventional heat pipes often face limitations, particularly in achieving higher heat dissipation rates and maintaining effective operation over longer transport distances. The wick structure in traditional heat pipes poses a significant challenge, as it restricts the transport distance and increases manufacturing complexity [2]. To overcome these limitations, the concept of the pulsating heat pipe (PHP), also known as the oscillating heat pipe (OHP), has been

\* Corresponding author.

E-mail address: [satish.kumar@me.gatech.edu](mailto:satish.kumar@me.gatech.edu) (S. Kumar).

introduced. PHPs are wickless, passive heat pipes composed of serpentine capillary tubes and are divided into three distinct sections: an evaporator (heat source), an adiabatic section, and a condenser (heat sink) [3]. This unique design allows PHPs to achieve superior thermal performance, making them a promising solution for low power electronic applications [4,5]. Unlike conventional designs, PHPs utilize the oscillatory motion of liquid slugs and vapor bubbles for passive heat transfer. Heat at the evaporator generates vapor, creating pressure that drives liquid toward the condenser. This motion compresses condenser vapor bubbles, generating a restoring force that pushes liquid back to the evaporator. When designed properly, this cycle sustains oscillations, enabling efficient heat transfer [6]. Unlike wicked and loop heat pipes, PHPs simplify system design by eliminating the need for a wick structure. PHPs are also less sensitive to the liquid wetting angle of the casing material relative to wicked heat pipes because the primary mechanism of liquid motion is not wicking [7].

PHPs can typically be designed in various configurations, such as open-loop systems, closed-loop systems, or closed-loop systems with added flow control check valves [8]. Over the years, numerous studies have been carried out to assess the performance of PHPs by altering the parameters that influence their performance. The thermal resistance of PHPs has been evaluated using different working fluids, varied levels of heat supply, and multiple fill ratios [9,10]. These studies have significantly contributed to understanding how changes in these parameters impact the behavior of PHPs, particularly in terms of their thermal resistance and overall performance. However, PHPs with fewer evaporator sections, which is correlated to the number of turns in common PHP designs [11], fail to operate effectively in horizontal orientations due to the lack of gravity assistance [12]. While adding check valves [13] can direct the working fluid in a specific direction, or increasing the number of turns [8] can improve performance, these solutions can be difficult and costly to implement, particularly when miniaturizing the PHP device. Uneven tube diameters or geometries in the adiabatic sections are introduced to create additional unbalanced capillary forces, addressing the operational challenges of PHPs with fewer turns [14]. Additionally, a figure of merit has been proposed by Qu et al. to guide the orientation-independent operation of an PHP with a dual-diameter channel [15]. These advancements provide valuable insights into overcoming the limitations of PHPs, paving the way for more efficient and versatile designs.

Flat plate PHPs, which are used in some industrial applications, are more challenging to manufacture compared to U-tube-based PHPs. Traditional manufacturing methods for flat plate PHPs require specialized machining techniques such as vacuum brazing and diffusion bonding. In recent years, additive manufacturing (AM) has become increasingly popular across various industries, providing a streamlined method for fabricating intricate three-dimensional structures using a wide variety of materials including polymers, ceramics, and metals [1,16–19]. AM technology eliminates the need for cutting tools or specific processing techniques, directly manufacturing complex 3D-parts by slicing and supporting the design of 3D-CAD files, thus streamlining the manufacturing process [20]. This approach has also been utilized in the design and fabrication of PHPs. Previous works have used additive manufacturing to produce PHPs with materials like Polycarbonate, Aluminium, ABS, Graphene-Laden PLA, and Ti-6Al-4V [21–24,25]. To address the low thermal conductivity of plastic materials in 3D printing, Koito et al. [25] developed a polymer PHP by 3D-printing it directly onto a thin polymer sheet, integrating the channel structure during the printing process. In their study, Koito and Kawaji [23] utilized polylactic acid (PLA) to fabricate a plastic PHP and explored its thermal behavior under low power inputs. Likewise, Koito and Hideyama [24] constructed a PHP from ABS polymer and assessed its heat transfer characteristics using HFE-7100 as the working fluid. The Selective Laser Melting (SLM) technique has also been used to fabricate and evaluate PHPs, leveraging its material versatility, high density, and tunable laser parameters for additive manufacturing suitability [20]. One of the

foundational investigations into SLA-based 3D printing of PHPs was carried out by Candere et al. [1]. Their study offered an extensive comparison with other major 3D-printing techniques, namely Fused Deposition Modeling (FDM) and Selective Laser Sintering (SLS). They employed Stereolithography (SLA) 3D-printing to fabricate polymeric PHPs, utilizing its precision and flexibility to produce intricate channel geometries, including channel non-uniformities, to improve performance. This method produces low mass, low-cost, and electrically insulating PHPs while providing high design versatility. However, it requires maintaining the average evaporator temperature below 80 °C to preserve the integrity of the photopolymer resin used [1]. Additionally, one significant advantage of using the resin in PHPs is their transparency, which facilitates efficient visualization experiments to better understand fluid flow inside the channels. Numerous researchers have also studied the fluid and vapor movements within PHPs, observing enhanced fluid motion due to dual-diameter channels [26]. Luo et al. examined nucleation and bubble growth at various power levels [27], while Patel et al. utilized visualization techniques to classify major flow patterns within a channel [3].

In this study, a flat plate closed-loop PHP is experimentally investigated, which is fabricated using SLA 3D-printing technology with Formlab's high-temperature transparent resin. Unlike metal-based PHPs with high thermal conductivity, this resin-based PHP aims to balance thermal conductivity with design flexibility and manufacturing costs [1]. Moreover, the resin's dielectric nature offers an advantage over metals in applications requiring electrical insulation, while its lightweight properties enhance suitability for weight-sensitive applications, particularly in portable or wearable devices [1]. Building on our previous work [16], where we examined a centrally heated PHP with two turns and highlighted the need for a higher number of turns to achieve startup in any orientation, this study additionally explores the thermal behavior of 10-loop PHPs. Experiments are conducted by heating acetone up to 100 °C and DI water up to 125 °C, and to the best of the authors' knowledge, no prior study has investigated SLA 3D-printed PHPs at such a high temperature. This study also examines the impact of evaporator positions on thermal resistance and fluid movement. Inspired by the advantages of dual-diameter channels, a novel channel design is introduced, where the diameters are modified at the evaporator locations—resulting in dual-diameters within a single channel for the center-heated PHP and alternating diameters for the end-heated PHP. This design induces uneven capillary forces, enhancing fluid movement and improving thermal performance [14,15,28]. To further understand the role of gravity in PHP operation, experiments are conducted, and startup is achieved in both vertical and horizontal orientations. For such resin-based SLA 3D-printed PHPs, which have lower thermal conductivity than metal-based counterparts, no study has reported successful startup with sustained oscillations in a horizontal orientation. Visualization techniques are employed to analyze differences in flow patterns, bubble growth, and fluid movement between end-heated and center-heated PHPs. Lastly, a study is conducted to evaluate heat loss due to conduction between the PHP surface and acetone, providing insights into the maximum power dissipation capacity of the PHPs.

## 2. Fabrication and design

Additive manufacturing (AM) has revolutionized fabrication by enabling the creation of highly intricate and complex geometries. A key factor in its widespread adoption is the availability of a diverse range of polymers in filament, powder, and resin forms, making it a versatile manufacturing technique. Among the various polymer-based 3D-printing methods, fused deposition modeling (FDM), selective laser sintering (SLS), and stereolithography (SLA) are commonly utilized. Candere et al. provided a thorough comparison of these methods, focusing on eight specific criteria: working principle, dimensional accuracy, surface roughness, resolution, build time, post-processing, ease of use, and cost [1].

This study used an SLA printing process to produce PHPs, leveraging its ability to achieve smooth surface finishes, high resolution, improved build quality, and efficient printing speed. The quality and accuracy of the final product depend on various factors. For SLA printers, critical parameters include the type of resin used, the LCD screen resolution, the layer thickness, the initial and subsequent exposure times, the cleaning method, and the final curing process [1,29]. The fabrication of PHP models was carried out using the Elegoo Saturn: 3 SLA printer. The printer features a 10-inch LCD screen with a resolution of  $11520 \times 5120$  pixels (12 K resolution) and supports printing dimensions of  $219 \times 123 \times 250$  mm with an XY resolution of  $19 \mu\text{m}$ . Screen-based SLA printers project an image to cure an entire layer of a part, this is distinct from laser-based SLA printers which use a laser to cure a single voxel (3-dimensional pixel) at a time.

Formlabs High Temp resin was used to increase the maximum operating temperature and heat flux of the PHPs. In polymer-based PHPs, the maximum material temperature plays a crucial role in determining the maximum heat flux, as the temperature drop across the solid walls of the device is comparable to the temperature drop across the fluid channels. This is due to the inherently low thermal conductivity of polymers. As a result, polymer PHPs have a built-in thermal resistance limit, since even if the fluid channel operates isothermally, heat must still transfer through the polymer walls, which present significant thermal resistance. Reducing the wall thickness can help lower this resistance; however, the structural limitations of polymers impose a minimum thickness that can be used. As the heat flux entering the PHP increases, the surface temperature rises significantly, sometimes causing the casing to reach its maximum material temperature before the PHP has a chance to start up. This presents a unique set of design challenges compared to metal-cased PHPs, where the temperature drop across the evaporator and condenser walls is much less significant. The values of thermal conductivity and coefficient of thermal expansion of this resin are  $\sim 0.28 \text{ W/m.K}$  and  $118.1 \times 10^{-6} \text{ }^{\circ}\text{C}^{-1}$  ( $0\text{--}150 \text{ }^{\circ}\text{C}$ ), respectively. This material was selected because of its transparency, stability at higher temperatures, and chemical resistance to common PHP working fluids.

The printer parameters were developed through trial and error with starting points from online forms, as Formlabs does not support the use of its resins in other SLA systems. The layer thickness was set to  $50 \mu\text{m}$ , the exposure time was 6 s, and the bottom exposure time was 20 s. Initial prints used longer exposure times and resulted in clogged channels. It was found that the printed channel heights were much smaller than the CAD design, and in some locations, the channel had collapsed completely. Exposure times below 6 s resulted in print failures due to lack of adhesion. To produce the desired channel depth of approximately 2.5 mm, the height of the channel in the CAD design had to be artificially increased to 4.5 mm, as shown in Table 1. This channel height error is an order of magnitude higher than what was observed by Candere et al. [1]. This could be due to the exposure time required to cure Formlabs High Temp Resin, which is double that used to cure the resin used by Candere et al., which may allow UV light to travel deeper into the resin pool than intended, partially curing resin in areas that were designed to be part of the PHP channel. Another possibility is that the screen-based 3D printing process used here is less effective at obtaining accurate Z heights relative

to the laser-based process used by Candere et al. [1]. This difference could be driven by the quality of the collimation process, which focuses on the UV light. Like the height of the channel, other dimensions of the print also differ from the CAD model. These dimensions have been summarized in Table 1.

In the PHP fabrication process, channels must be kept small enough to fit several turns. Several turns are needed to stabilize oscillations [8]. If channels are too small, it becomes difficult to remove resin from the channels, and small manufacturing defects lead to blocked channels. Additionally, smaller distances between adjacent channels allow more channels to be added to the PHP. During the development of the PHP design, it was desired to minimize the distance between adjacent channels; however, it was discovered that small openings between channels occur when the space between channels is less than 2 mm. This could be a result of the high viscosity of the resin used relative to other resins, which may prevent the resin from spreading over the part surface prior to the curing of that layer begins. To alleviate this issue, the retraction speed of the build plate was slowed and the wait time after retraction was increased to provide more time for the air bubbles to escape, however, these changes did not reduce the occurrence of connections between adjacent channels. A minimum spacing between channels of 2 mm was set as a constraint to avoid unwanted channel connections.

After the print is completed, the part is removed from the build plate, and uncured resin must be removed from the PHP channels. The design of the PHP included several holes to streamline the removal of excess resin. This process required using a vacuum system to remove the excess resin before exposing the part to isopropyl alcohol (IPA) for approximately 12 h to reduce the viscosity of the uncured resin before repeating the vacuum operation. This process was continued 3 times before the PHP was flushed with water. The resin removal process was significantly more intensive due to the high viscosity of Formlabs High Temp resin relative to other SLA resins. Finally, the PHP was sealed by manually filling the resin removal holes with the same resin and using a handheld UV light to partially cure the filling resin in place before moving it to a UV curing oven, where the entire PHP was cured.

The three fabricated PHP designs include the 2-Turn Center-Heated PHP (2T-C), the 10-Turn Center-Heated PHP (10T-C), and the 10-Turn End-Heated PHP (10T-E), all of which share a uniform channel length of 134 mm. The 2T-C has two loops forming four channels, while 10T-C and 10T-E have ten loops forming twenty channels. All three designs incorporate a dual-diameter channel configuration common in the literature [1,14,15,28], but in different ways. The 10T-E follows a common end-heated configuration where alternating channels have different widths, a design explored in previous studies. In contrast, 2T-C and 10T-C employ a configuration where each channel features two different widths along its length. As far as the authors are aware, this adaptation of dual-width configuration is novel. In the center-heated PHPs (2T-C and 10T-C), a 10 mm transition length at the center causes alternating channel widths—2 mm and 1 mm in 10T-C, and 3 mm and 2 mm in 2T-C—ensuring no adjacent channels share the same cross-section. In the end-heated PHP (10T-E), this transition occurs at the ends, resulting in uniform cross-sections along each channel while alternating between widths in adjacent channels. Figs. 1 and 2 illustrate the channel configurations of 10T-C and 10T-E, respectively, while the 2T-C channel configuration, similar to 10T-C, can be found in our previous work [16]. The 10T-C configuration, shown in Fig. 1(a), features a center-heated layout in which the evaporator section is positioned symmetrically between two condenser sections. This design results in bidirectional heat transport and symmetrical flow paths. This design also doubles the number of individual evaporator and condenser sections along the channel path, which promotes oscillatory stability. Fig. 1 (b) presents the image of the fabricated 10T-C PHP, which was manufactured using a high-temperature resin through the SLA 3D-printing process.

**Table 1**  
The dimensions of channel geometry.

Configurations	Channel-1 width (mm)	Channel-2 width (mm)	Channel height (mm)	Spacing between channels (mm)	Wall thickness (mm)
2T-C	2 (1.85)	3 (2.67)	3 (1.23)	4 (3.82)	1 (2.245)
10T-C	1 (0.7874)	2 (1.9558)	4.5 (2.3622)	2.3 (2.032)	1 (2.2098)
10T-E	1 (0.62)	2 (1.6)	4.5 (2.51)	2.2 (2.3)	1 (2.415)

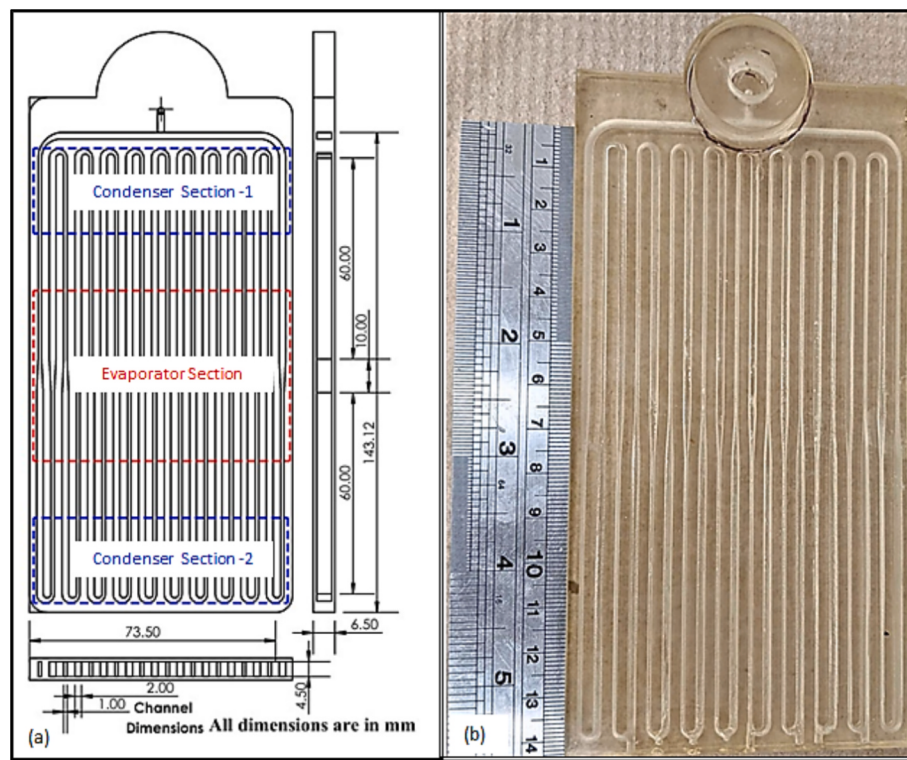


**Fig. 1.** (a) Schematic of the 10T-C fabricated using 3D-printer and (b) image of a fabricated PHP.

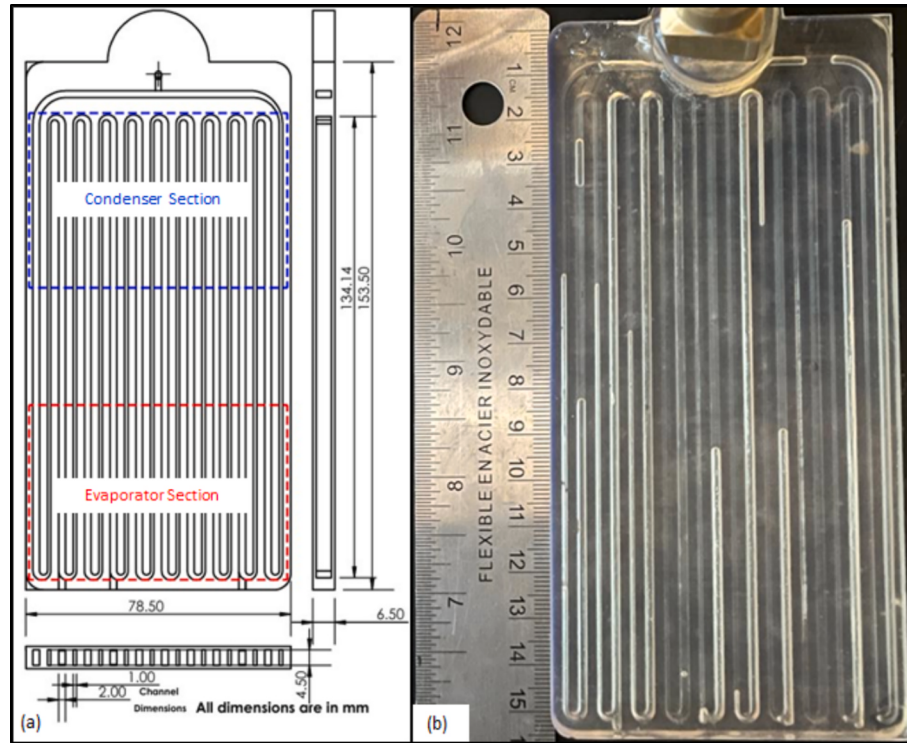


**Fig. 2.** (a) Schematic of the 10T-E fabricated using 3D-printer and (b) image of a fabricated PHP.

### 3. Test setup and data processing

#### 3.1. Experimental apparatus

In this study, experiments were conducted on 2T-C, 10T-C, and 10T-

E in both horizontal and vertical orientations. [Fig. 3](#) illustrates the layout of the test setup, including the evaporator, condenser, cooling loop, vacuum system, and data acquisition unit for the center-heated configuration. The primary difference in the end-heated setup is that the evaporator section was relocated at one end of the PHP, away from the

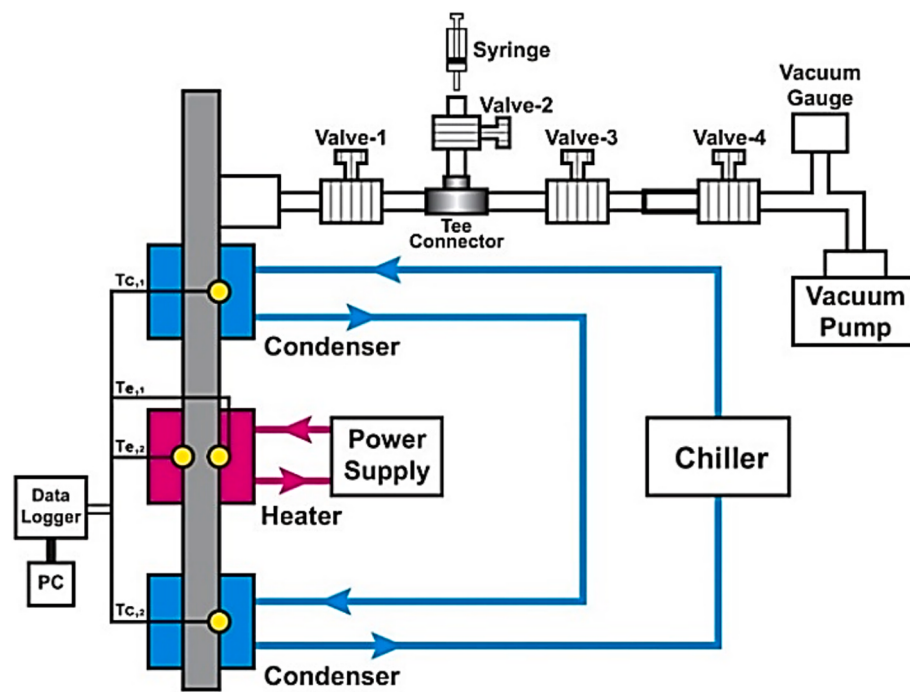


Fig. 3. Schematic diagram of the experimental setup for center heating mode [16].

charging port, while the condensers were repositioned at the opposite end as shown in Fig. 2(a).

Electric heating in the evaporator section was facilitated through two surface heaters, one mounted on the top surface and the other on the bottom. Each heater was mounted onto copper plates of equal size to improve heat distribution. This has a significant impact on the boundary condition of polymer PHPs because the low thermal conductivity of the casing material inhibits axial conduction, which increases the likelihood of localized dry-outs and device failure. The power supply capacity of the heater was 20 W for the 2T-C and 60 W for both the 10T-C and 10T-E. Throughout the testing process, the power supply provided heating up to 6.5 W, 22.1 W, and 38.5 W for the 2T-C, 10T-C, and 10T-E experiments, respectively. The condenser section featured four cooling blocks, with each circulating distilled water at  $78.3 \text{ cm}^3 \text{ s}^{-1}$  with a fixed temperature of 10 °C. All the configurations used the same heating and cooling boundary conditions on each side of the PHP channels, with the exception of the visualization studies, which only used heating and cooling blocks on one side. Heating and cooling blocks were used to achieve the desired evaporator and condenser dimensions. For the 2T-C configuration, an evaporator located at the center of the channels was 25.4 mm × 25.4 mm, and two condensers located at either end also measured 25.4 mm × 25.4 mm. The 10T-C configuration featured an

evaporator located at the center of the channels measuring 76.2 mm × 50.8 mm and two condensers located at either end measuring 76.2 mm × 25.4 mm. For the 10T-E configuration, an evaporator was located at the end of the channels and measured 76.2 mm × 50.8 mm, while a condenser of equal size was positioned at the opposite end of the channels. In this study, relatively large evaporators and condensers were used to increase the heat transfer area through the resin. This is especially critical because of the low thermal conductivity of the resin. This is also the reason the PHPs were heated and cooled from both sides in some of the experiments. The geometric and operating parameters for all three considered configurations are presented in Table 2.

K-type thermocouples were employed to capture temperature variations at four specific locations in the PHP—two in the evaporator section and two in the condenser section. Their positioning is illustrated in Fig. 3. Prior to experimentation, all thermocouples underwent calibration, ensuring a measurement accuracy of  $\pm 0.5$  °C. The acquired signals were digitized by the data acquisition system, recorded at a sampling rate of 1 Hz, and transferred to the host computer for further processing.

Table 2  
Description of geometric and operating parameters.

	Parameter	2T-C	10T-C	10T-E
<b>Geometric Parameters</b>	Number of turns	2	10	10
	Evaporator size (mm × mm)	25.4 × 25.4	76.2 × 50.8	76.2 × 50.8
	Number of evaporators per side	1	1	1
	Condenser size (mm × mm)	25.4 × 25.4	76.2 × 25.4	76.2 × 50.8
	Number of condensers per side	2	2	1
<b>Operating Parameters</b>	Working fluid	Acetone	Acetone	Acetone/Water
	Fill ratio (%)	51	59	55
	Inlet temperature of condenser [°C]	10	10	10
	Flow rate of coolant in each cooling block [ $\text{cm}^3/\text{s}$ ]	78.3	78.3	78.3
	Heating mode	Center	Center	End
	Orientation	Vertical-Horizontal	Vertical-Horizontal	Vertical-Horizontal/Vertical
	Terminal temperature [°C]	100	100	100/125

### 3.2. Experimental procedure

The PHP working fluid was degassed by subjecting it to vacuum conditions and isolating the liquid phase with a syringe and valve assembly. The PHP was first evacuated using a vacuum pump to eliminate non-condensable gases from the system, as illustrated in Fig. 3. After evacuation, the working fluid was injected into the PHP using a syringe through a valve close to the filling port. The valve was then closed, ensuring the PHP functioned as a fully independent closed-loop system. The system was confirmed to be used repeatedly without leaks, provided that the evaporator section temperature did not exceed 100 °C, beyond which structural integrity could be compromised. It is believed structural issues above 100 °C were caused by chemical attack by acetone at elevated temperatures, which led the structure to become noticeably more brittle over time. Preliminary tests with water as the working fluid found the casing maintained structural integrity temperatures as high as 150 °C.

Acetone was selected as the primary working fluid in this study due to its low startup power requirement and moderate vapor pressure, which reduces mechanical stress on the casing compared to alternative refrigerants such as R134a. To benchmark its performance, deionized (DI) water was also tested in a single case with a fill ratio of 55 %. A fill ratio of 55 % was targeted for each test. The exact fill ratio of each test was determined through mass measurements. The resulting fill ratios for different configurations were 51 % for the 2T-C, 59 % for the 10T-C, and 55 % for the 10T-E as shown in Table 2.

During the experiment, the input power was supplied via DC power supply, which enabled fine control of heat input to the evaporator section. Electrical resistance heaters were mounted on copper plates that were attached to the PHPs. The heater assemblies were well insulated before they were clamped to the PHPs to avoid heat losses through clamping connections. The cooling system consisted of a recirculating chiller connected to condenser blocks, maintaining a constant setpoint temperature during experiments. Temperature data were collected using thermocouples across the evaporator and condenser sections, and these signals were fed into a multi-channel data logger connected to a PC for real-time monitoring and post-processing. The input power was gradually increased in increments, and at each level, the PHP temperature distribution was monitored to confirm steady-state conditions. A system was considered to reach a steady state when the average temperature data remained within ±0.5 °C over a 5-minute duration. To safeguard against overheating, the power supply was manually switched off once the evaporator section exceeded the terminal temperature considered. The experimental procedure involved testing the charged PHP in both horizontal and vertical orientations. To establish a baseline for comparison, an uncharged PHP was also subjected to testing.

### 3.3. Heat loss calculations

Polymer PHPs typically have higher thermal resistance compared to metal PHPs due to the low thermal conductivity of the casing material. The higher thermal resistance makes it more likely that a substantial proportion of the electrical energy dissipated by the PHP heaters is lost to the environment, even when insulation is used. The heat loss from the heater plates attached to the PHP must be approximated to accurately determine the heat load transported by the PHP. The experimental setup was covered by a uniform layer of fiberglass insulation of approximately 1 in. To characterize the heat loss, a constant thermal resistance per unit area,  $R_\infty$  with units  $\frac{m^2 K}{W}$ , was calculated based on results from experiments using an empty PHP and the known thermal conductivity of the material.  $R_\infty$  includes the resistance to heat transfer due to the insulation and due to free convection to the environment.

To determine the heat loss, multiple trials were conducted without working fluid in the PHP. The condenser blocks were run under the same conditions as the other experiments, and small amounts of power were

dissipated by the heaters. The system was allowed to reach steady-state, and the average evaporator and condenser temperatures were recorded. The empty PHP is treated as one-dimensional, which allows the temperature across the PHP to be defined. The evaporator section and condenser section are assumed to be at a constant temperature due to the high thermal conductivity of the copper heating and cooling blocks. Average evaporator and condenser temperatures,  $\bar{T}_e$  and  $\bar{T}_c$ , are determined by averaging the steady-state temperatures measured in those locations. The temperature in the adiabatic section is a function of location and is determined according to the analytical fin equation for the case where the temperature of the fin base is known [30]. A schematic of the system is shown in Fig. 4.

The total heat dissipated by the heaters, which is measured electrically, is given by

$$Q_{elc} = 2Q_{cnd} + Q_{loss} + 2Q_{loss_{adb}} \quad (1)$$

where  $Q_{cnd}$  and  $Q_{loss_{adb}}$  are multiplied by a factor of 2 because there are 2 adiabatic sections and 2 condenser sections.  $Q_{loss}$  is the heat lost from the evaporator sections and is given by

$$Q_{loss} = A_e \frac{(T_e - T_\infty)}{R_\infty} \quad (2)$$

and  $Q_{loss_{adb}}$  is determined with a common analytical conduction solution for a fin with a prescribed base temperature, i.e.

$$Q_{loss_{adb}} = (T_e - T_\infty) w \sqrt{h^* per k_r A_c} \frac{\left( \cosh(mL) - \left( \frac{T_c - T_\infty}{T_e - T_\infty} \right) \right)}{\sinh(mL)} \quad (3)$$

where  $L$  is the length of a single adiabatic section,  $k_r$  is the thermal conductivity of the resin material,  $m$  is given by

$$m = \sqrt{\frac{h^* per}{k_r A_c}} \quad (4)$$

$h^*$  represents an effective convection coefficient over the fin equivalent to  $\frac{1}{R_\infty}$ .  $Q_{cnd}$  is given by

$$Q_{cnd} = k_r A_c \frac{dT}{dx} \Big|_{x=L} \quad (5)$$

where  $\frac{dT}{dx}|_{x=L}$  can be found by differentiating the temperature profile in the adiabatic section, which is part of the analytical fin solution, yielding

$$\frac{dT}{dx} = m(T_e - T_\infty) \left[ \frac{\left[ \frac{T_c - T_\infty}{T_e - T_\infty} \right] \cosh(mx) - \cosh(m(x-L))}{\sinh(mL)} \right] \quad (6)$$

With this system of equations,  $R_\infty$  can be determined from uncharged experiments by using the accepted value for the casing material's thermal conductivity ( $0.28 \frac{W}{mK}$ ), and by calculating the cross-sectional area of the PHP casing material while accounting for the missing area due to the presence of the channels.  $R_\infty$  was calculated for 2T-C and 10T-C for a range of evaporator temperatures between 40 and 100 °C, and the average value across the temperature range was used to approximate the heat loss. A similar process was conducted for 10T-E, where Eq. (1) and the adiabatic section length was modified to account for the different geometry of 10T-E. The heat loss from the evaporator of each PHP can then be approximated by

$$Q_{loss} = f_{loss}(T_e - T_\infty) \quad (7)$$

where  $f_{loss}$  equivalent to  $\frac{A_e}{R_\infty}$ . The loss factors for 2T-C, 10T-C, and 10T-E were found to be 0.036, 0.074, and 0.098  $\frac{W}{k}$ , respectively. The heat transported into the PHP,  $Q_{in}$ , was then calculated by

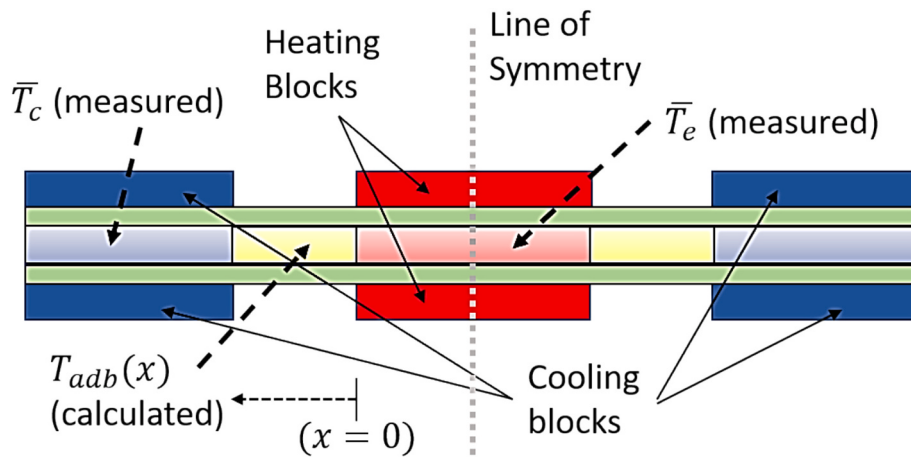


**Fig. 4.** Schematic of the PHP for heat loss estimation.

$$Q_{in} = Q_{elc} - Q_{loss} \quad (8)$$

It should be noted that heat that exits through the insulation in the adiabatic section(s) is considered to have been transported by the PHP and therefore is part of  $Q_{in}$ .

### 3.4. Uncertainty

The primary contribution of uncertainty in the present experiment is the approximation of heat losses to the ambient. To approximate the relevance of these losses in the analysis of PHP performance it is conservatively assumed the calculation of  $Q_{loss}$  is within 10 % of the true heat losses from the evaporator. This assumption allows  $U_{Q_{in}}$ , the uncertainty of  $Q_{in}$  to be calculated according to

$$U_{Q_{in}} = 0.1f_{loss}(T_e - T_\infty) \quad (9)$$

where the uncertainty due to errors in temperature measurement and  $Q_{elc}$  are included in 10 % error assumption because they are comparatively small.  $U_{Q_{in}}$ , therefore, increases linearly with the evaporator temperature. The maximum value of  $U_{Q_{in}}$  for 2T-C, 10T-C, and 10T-E, respectively was 0.24, 0.53, and 0.66 W for the cases where acetone was the working fluid. When 10T-E was tested with water, the higher maximum evaporator temperature resulted in a higher maximum  $U_{Q_{in}}$  of 0.98 W.

The uncertainty of thermal resistance  $U_{R_{th}}$  is calculated according to the general propagation of uncertainty rules, accounting for the uncertainty of  $Q_{PHP}$  and  $\Delta T_{avg}$

$$U_{R_{th}} = \frac{\Delta T_{avg}}{Q_{in}} \sqrt{\left(\frac{U_{\Delta T_{avg}}}{\Delta T_{avg}}\right)^2 + \left(\frac{U_{Q_{in}}}{Q_{in}}\right)^2} \quad (10)$$

where  $U_{\Delta T_{avg}}$  is 1 due to the 0.5 °C uncertainty in the measurement of both the evaporator and condenser measurement. Values of  $U_{R_{th}}$  are large in low heating cases, and shrink quickly as  $Q_{in}$  is increased. An example of the relative scale of uncertainty is given in section 4.8.

### 3.5. Data reduction

The thermal resistance of the PHP is evaluated by computing the ratio of the temperature difference between the average evaporating and condensing temperatures to the applied heat input. The definitions of these resistances vary depending on the heat input, the inclusion of heat loss ( $Q_{loss}$ ) in heat input, and whether the number of channels ( $n$ ) is considered. They are expressed as  $R_{elc}$ ,  $R_{th}$  and  $R_{th-ch}$ , where  $R_{elc}$  accounts for heat input excluding losses ( $Q_{elc}$ ),  $R_{th}$  considers heat input including losses ( $Q_{in}$ ), and  $R_{th-ch}$  represents the per-channel resistance

based on heat input with losses ( $Q_{in-ch}$ ).

$$R_{elc} = \frac{\Delta T_{avg}}{Q_{elc}} = \frac{T_{e,avg} - T_{c,avg}}{Q_{elc}}, \quad (11)$$

$$R_{th} = \frac{\Delta T_{avg}}{Q_{in}} = \frac{T_{e,avg} - T_{c,avg}}{Q_{in}}, \quad (12)$$

$$R_{th-ch} = \frac{\Delta T_{avg}}{Q_{in-ch}} = \frac{T_{e,avg} - T_{c,avg}}{Q_{in-ch}}, \quad (13)$$

$$\overline{T}_{ij} = T_{i,j-avg} = \frac{1}{300} \sum_{t=1}^{300} (T_{i,j})_t \quad (14)$$

$$T_{e,avg} = \frac{\overline{T}_{e,1} + \overline{T}_{e,2}}{2} \quad (15)$$

$$T_{c,avg} = \frac{\overline{T}_{c,1} + \overline{T}_{c,2}}{2} \quad (16)$$

$$Q_{elc} = V \times I \quad (17)$$

$$Q_{in} = Q_{elc} - Q_{loss} \quad (18)$$

$$Q_{in-ch} = \frac{Q_{in}}{n} \quad (19)$$

The variables  $T_{e,avg}$  and  $T_{c,avg}$  correspond to the average temperatures of the evaporator and condenser sections, respectively, with  $\Delta T_{avg}$  denoting the difference between them. In Eq. (14), the subscript  $t$  signifies the temperature recorded at the  $t$ -th second. The time-averaged temperature  $\overline{T}_{ij}$  is computed using 300 recorded values collected over a 5-minute period under steady-state conditions. The surface temperatures at the heating and cooling zones are expressed as  $T_{e,1}$ ,  $T_{e,2}$  for the evaporator and  $T_{c,1}$ ,  $T_{c,2}$  for the condenser, as shown in Fig. 3. The supplied voltage and current are represented by  $V$  and  $I$ , respectively.

## 4. Results and discussion

### 4.1. Thermal performance analysis of 2-turn PHP

Fig. 5(a) presents the variation of  $\Delta T_{avg}$  with respect to heat input excluding loss ( $Q_{elc}$ ) for the 2T-C PHP tested in vertical and horizontal charged conditions, along with the uncharged case for baseline comparison.  $Q_{elc}$  is used in these graphs to demonstrate the performance difference of each test relative to the uncharged case, as the actual heat transport  $Q_{PHP}$  is very low in the uncharged cases, leading to high uncertainty. Starting from around 1.2 W,  $\Delta T_{avg}$  exhibits a sharp increase

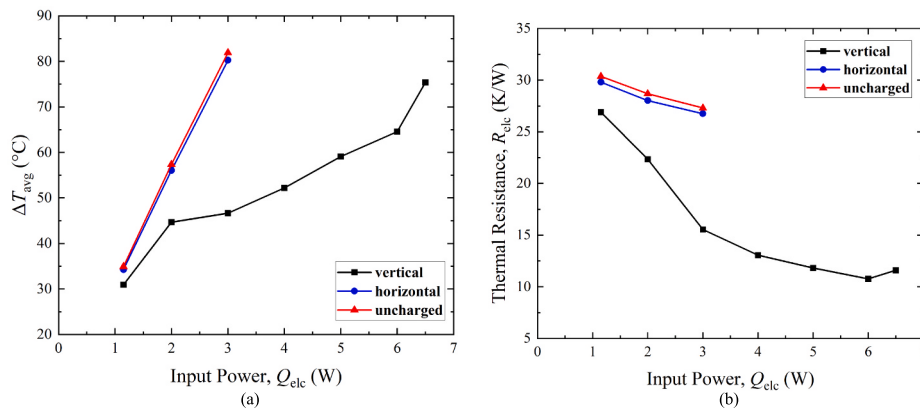


**Fig. 5.** Variation of (a)  $\Delta T_{avg}$  and (b) thermal resistance with heat input excluding loss for 2T-C PHP.

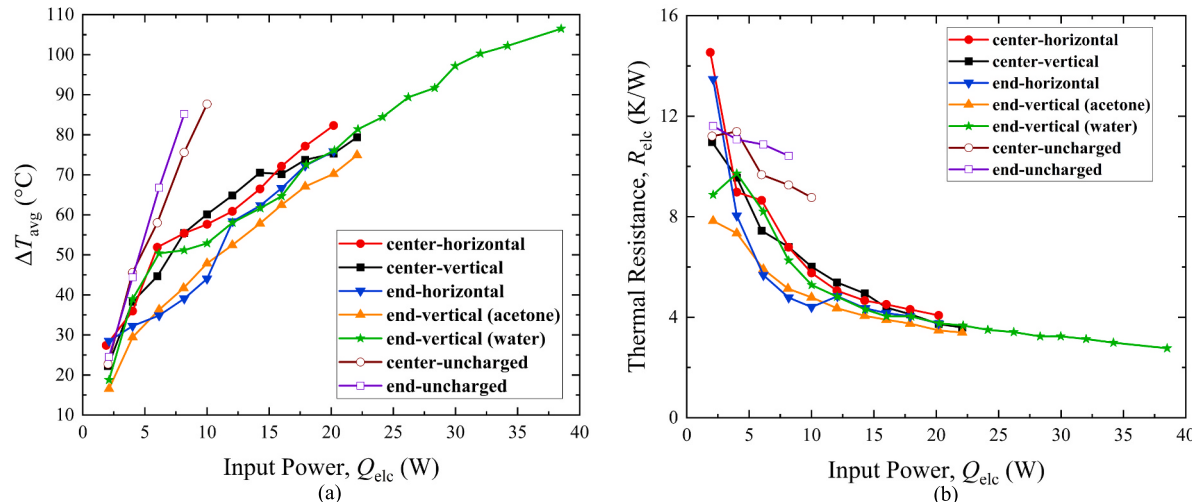
until reaching 2 W for vertical orientation. Following this rise,  $\Delta T_{avg}$  stabilizes at approximately 45 °C between 2 W and 3 W before undergoing another increase till 6.5 W. This observation indicates the startup point is at approximately 3 W. Conversely, the horizontally charged PHP behaves like the uncharged PHP, with  $\Delta T_{avg}$  increasing linearly and continuously from the beginning, while  $T_{e,avg}$  exceeds the terminal temperature of 100 °C beyond 3 W, denoting the absence of startup.

Fig. 5(b) illustrates corresponding plots for thermal resistance,  $R_{elc}$ . In the vertically charged PHP, a notable reduction in thermal resistance is observed once the input power exceeds 2 W, as the heating power starts the oscillatory motion of the working fluid within the channels. This onset of motion marks the beginning of thermal transport notably facilitated by phase-change dynamics. This trend continues up to 6 W, with thermal resistance steadily decreasing as oscillations strengthen and more fluid passes between the evaporator and condenser regions. In contrast, the uncharged and horizontally oriented PHPs show relatively flat trends, failing to exhibit such a decline in thermal resistance. The thermal resistance in the uncharged PHP remains within 30.4–27.3 K/W, while the horizontal charged PHP follows a similar trend at 29.8–26.8 K/W, failing to achieve a startup. In contrast, the vertical PHP starts up around 3 W and reaches a minimum resistance of approximately 10.8 K/W at 6 W, highlighting its superior thermal performance despite having only two turns. These observations are in agreement with prior studies, which report similar startup difficulties for horizontally oriented constant diameter PHP [8], and dual-diameter PHP with low numbers of turns with diameter changes [15].

Despite reaching a minimum resistance at 6 W, the vertical PHP exhibits a slight increase in  $R_{elc}$  beyond this point although the oscillatory flow persists. While this increase is within the range of experimental uncertainty, it could be due to the partial dry out that leads to failure or higher viscous flow resistance in the smaller channels, which becomes more significant at higher fluid velocities. This behavior aligns with the findings reported in [23]. In brief, these findings indicate that achieving startup in the horizontal orientation still requires a minimum number of turns, despite the presence of dual-diameter channels that introduce additional imbalance forces. This led to further investigations using higher-turn configurations, 10T-C and 10T-E, as detailed in section 4.2.

#### 4.2. Thermal performance analysis of 10-turn PHP

Fig. 6(a) illustrates the relationship between  $\Delta T_{avg}$  and  $Q_{elc}$  for the 10T-C and 10T-E across seven test configurations, encompassing both center- and end-heating modes, with vertical and horizontal orientations for each.  $Q_{elc}$  is again used for these graphs to compare with the uncharged cases. Unlike the 2T-C, where horizontal cases failed to start, all charged 10T-C and 10T-E exhibit startup and continue oscillatory operation, distinguishing them from the uncharged cases, which show a continuous rise in  $\Delta T_{avg}$  with no stabilization. While acetone serves as the working fluid for all charged tests, an additional experiment was conducted using water for the 10T-E vertical orientation, extending heating beyond the usual 100 °C limit to 125 °C. This resulted in an evaporator temperature of approximately 121 °C at 38.5 W, following a



**Fig. 6.** Variation of (a)  $\Delta T_{avg}$  and (b) thermal resistance with heat input excluding loss for 10T-C and 10T-E.

trend similar to that of the acetone test.

As depicted in Fig. 6(b), the thermal resistance ( $R_{elc}$ ) of the 10T-C and 10T-E demonstrates a clear decline with increasing  $Q_{elc}$  for all charged cases following startup, unlike their uncharged counterparts, which maintain higher values. The vertical and horizontal 10T-C PHPs perform similarly, with occasional intersections in their resistance curves. A similar trend is evident in the 10T-E cases, reinforcing the idea that higher-turn PHPs exhibit reduced dependence on gravity, leading to an orientation-independent resistance behavior. These findings are in agreement with previous studies [26,31,32].

The 10T-Es, in both vertical and horizontal orientations, demonstrate lower resistance than their 10T-C counterparts, with a more pronounced difference at lower power inputs until 10 W. Beyond 10 W, the resistance values converge across all charged configurations. This specific trend is explored further in a later section. Among all tested cases, the 10T-E vertical PHP consistently exhibits lower resistance at most points. A subsequent test using DI water in this configuration revealed a resistance trend mostly similar to its acetone counterpart, though slightly higher at equivalent heat inputs. A detailed discussion of this working fluid-based performance difference is presented in section 4.5.

#### 4.3. Comparative analysis of center-heated 2-turn and 10-turn PHPs

To compare the PHPs with more detail and precision based on turn count, geometry, orientation, and heat load, analysis is conducted accounting for the heat losses from the evaporator to the surroundings as described in section 3.3. In Fig. 7, the thermal performance of the 2T-C and 10T-C configurations is compared to analyze the effect of turn count by considering heat input per channel ( $Q_{in-ch}$ ) and thermal resistance per channel ( $R_{th-ch}$ ).

As shown in Fig. 7(a), with heat input per channel adjusted to account for losses, the  $\Delta T_{avg}$  graph highlights the performance differences among configurations. The 10T-C vertical and horizontal PHPs follow comparable  $\Delta T_{avg}$  trends, as  $Q_{in-ch}$  rises from 0.1 W to around 0.9 W per channel. In contrast, the 2T-C vertical PHP demonstrates a consistently lower  $\Delta T_{avg}$  for all input power levels, extending up to approximately 1.0 W per channel.

Referring to Fig. 7(b), the thermal resistance per channel ( $R_{th-ch}$ ) decreases with increasing heat input per channel ( $Q_{in-ch}$ ), indicating improved heat dissipation at higher power levels. The 10T-Cs in both orientations exhibit nearly identical resistance trends, with occasional intersections within the experimental uncertainty range, suggesting that orientation has minimal influence when the number of turns is

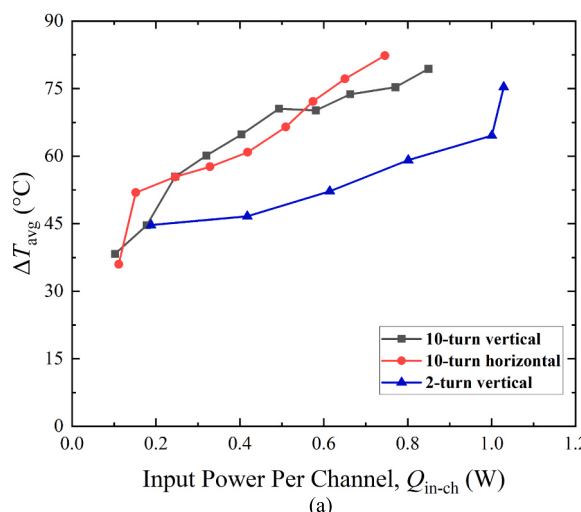


Fig. 7. Comparison of (a)  $\Delta T_{avg}$  and (b) thermal resistance per channel for 2T-C and 10T-C.

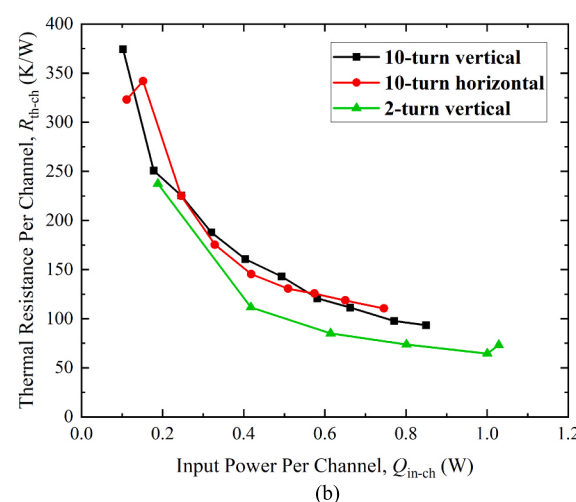
sufficiently high. In contrast, the 2T-C vertical PHP exhibits lower resistance across all heat input levels per channel, reaching a minimum of approximately 65 K/W at 1 W. While the previous total system resistance analysis (Figs. 5 and 6) indicated higher values for the 2T-C in the vertical orientation, the per-channel approach shows that the 2T-C achieves lower resistance per channel. This observation is unusual, as most researchers report improved performance when increasing the number of channels. It is likely the superior performance of the 2T-C vertical PHP is due to the wider channel size compared to the 10T-C, which reduces the conduction resistance between the outer PHP wall and the PHP channel wall substantially. A 2D computational conduction study was completed that indicated a 39 % increase in conduction resistance per channel in the 10T-C compared to 2T-C. This difference is likely magnified by the operation of the PHP, as increasing the axial heat flux through the channels at a fixed operating temperature generally improves the PHP resistance when the axial heat flux is low [33]. It should be noted that the average channel cross-sectional areas in 2T-C and 10T-C are essentially equal due to the reduced height of the channels in 2T-C. This observation demonstrates how small changes in casing and channel geometry can have a significant impact on performance.

#### 4.4. Performance comparison between center-heated and end-heated modes

This analysis explores the effect of different heating modes on the 10-turn PHP in both horizontal and vertical orientations, incorporating heat loss in the input power.

Fig. 8(a) presents the variation of  $\Delta T_{avg}$  with  $Q_{in}$  for 10T-C and 10T-E, tested in vertical and horizontal orientations. The 10T-C horizontal PHP exhibits the highest  $\Delta T_{avg}$ , reaching approximately 82  $^{\circ}$ C at 14.9 W, followed closely by the 10T-C vertical PHP. The 10T-E PHPs, in contrast, exhibit lower  $\Delta T_{avg}$  values for most instances, with the vertical case maintaining a slightly lower temperature than its horizontal counterpart, especially at higher power inputs.

As shown in Fig. 8(b), the thermal resistance ( $R_{th}$ ) of all configurations decreases as heat input increases, demonstrating improved heat dissipation. All tested PHPs successfully initiated startup, with startup occurring near 3.5–5 W for 10T-C cases and slightly lower, around 3.4–3.6 W, for 10T-E cases. The 10T-C vertical and horizontal PHPs display nearly identical resistance curves, with minor intersections that are not significant relative to the experimental uncertainty described in the upcoming section 4.8. The 10T-E PHPs demonstrate significantly lower resistance at lower power inputs, up to around 6.5 W, for both horizontal and vertical orientations. This difference is larger than the



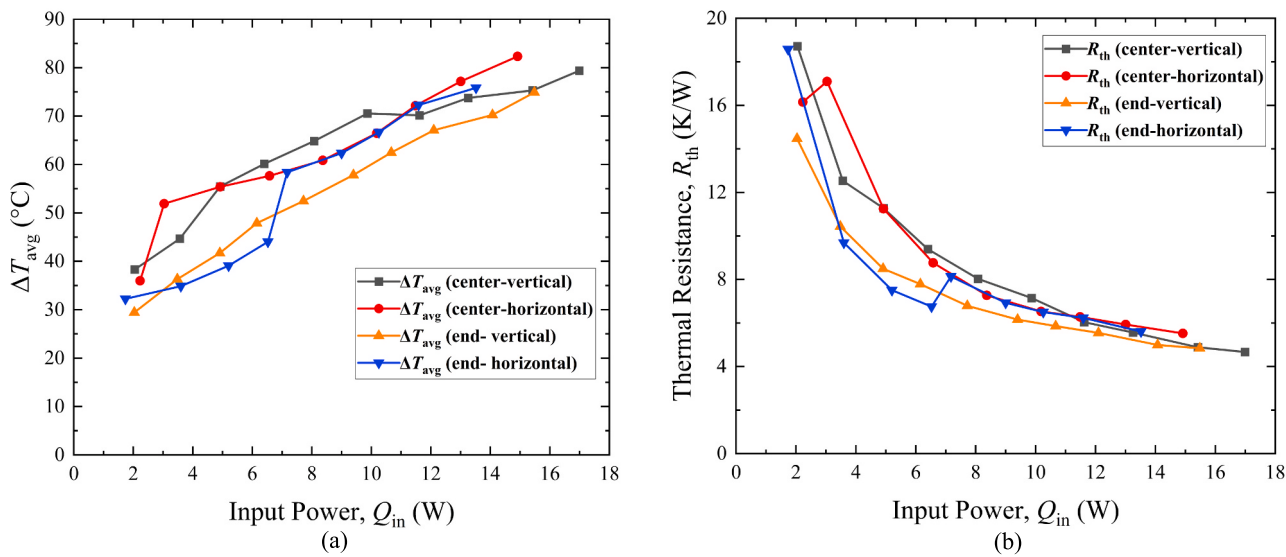


Fig. 8. Comparison of (a)  $\Delta T_{\text{avg}}$  and (b) thermal resistance in 10-turn PHP for two heating modes.

experimental uncertainty. The superior performance in the 10T-E case is unusual because 10T-C PHPs generally have better performance, due to the doubling of condenser sections along the PHP channel, and that the PHP heat load is distributed in two directions [34]. This difference could be explained by the visualization studies in the later section 4.6, which shows 10T-C operating with intermittent oscillations in the relevant heating range, while 10T-E operates with steady oscillation. The different operating modes could be attributed to the different number of condenser sections. Yoon and Kim [35] observed a phase shift between liquid slugs and in a subsequent study, Lee et al. [36] found that when the number of heated sections was sufficient, the cumulative effect of the phase shift in each liquid slug led to larger scale oscillations at a reduced frequency. It is possible that the larger number of heated sections in 10T-C led the system to operate at a lower frequency, but the axial heat flux through the PHP and therefore the rate of vapor generation was not sufficient to maintain the larger oscillations as described by Pawlick [37]. In this case, it appears that steady small amplitude oscillations resulted in better performance than intermittent oscillations with larger amplitudes. This behavior demonstrates another complexity of PHP operation at low heat fluxes and is likely sensitive to experimental details such as geometry, working fluid, and operating temperature.

Beyond 6.5 W of  $Q_{\text{in}}$ , resistance values become more comparable between 10T-E and 10T-C cases, with the 10T-E vertical configuration retaining a slightly lower value. This could be explained by the transition of 10T-C and 10T-E to the same oscillation type resulting in increased resistance in 10T-E. When  $\Delta T_{\text{avg}}$  remains between 75  $^{\circ}\text{C}$  and 83  $^{\circ}\text{C}$ , marking the experiment's final phase, all PHP configurations exhibit nearly identical resistances, with a maximum variation below 1 K/W. This suggests that PHP operation becomes largely independent of orientation and heating mode at higher power levels, which is consistent with the results of Lee et al. [36]. Further validation could be achieved by testing the PHP at even higher terminal temperatures. Among all configurations, the 10T-C vertical PHP reached the highest power input of 17 W, slightly surpassing the 10T-E cases, and recorded the lowest resistance of around 4.7 K/W.

#### 4.5. Working fluid-based performance evaluation

This study employs acetone as the working fluid for all configurations, considering a maximum evaporator temperature of 100  $^{\circ}\text{C}$ . For thermal performance comparison, deionized (DI) water is chosen because of its compatibility with the resin material and easy availability, despite its lower vapor pressure. Unlike acetone testing, the terminal

temperature for this test was set at 125  $^{\circ}\text{C}$  with a fill ratio of 55 %, as previously mentioned. The 10T-E vertical configuration is chosen as PHPs charged with water are known to perform well in this configuration, while PHPs charged with water in the horizontal orientation often fail to start up [38]. The performance of 10T-E charged with water and acetone is compared in Fig. 9.

In Fig. 9(a), the  $\Delta T_{\text{avg}}$  variation for acetone and DI water in the 10T-E vertical orientation is depicted. The  $\Delta T_{\text{avg}}$  trends are similar for both fluids, with water exhibiting consistently higher temperature differences at equivalent power inputs. While using acetone, following previous test conditions, temperature was limited to 100  $^{\circ}\text{C}$ , while the water-charged PHP continued heating till 125  $^{\circ}\text{C}$ .  $\Delta T_{\text{avg}}$  peaked at 106.5  $^{\circ}\text{C}$  at nearly 28.7 W for water, while acetone reached  $\sim 75$   $^{\circ}\text{C}$  at around 15.5 W.

As depicted in Fig. 9(b), the thermal resistance behavior of the PHP follows a similar decreasing trend for both fluids as input power increases. While both fluids exhibit similar overall behavior, water consistently presents slightly higher thermal resistance than acetone at corresponding heat inputs. Startup was observed at around 4 W for water, with  $R_{\text{th}}$  value of approximately 12.7 K/W, while acetone exhibited an earlier startup at nearly 3.5 W with a lower resistance value of 10.4 K/W. This delay in startup is consistent with the prior observations of authors and can be attributed to the lower vapor pressure and higher latent heat of water relative to acetone [39]. Acetone showed slightly lower resistance throughout for the comparable heat input up to  $\sim 15.5$  W. As water was heated PHP temperature increased until 125  $^{\circ}\text{C}$ ,  $R_{\text{th}}$  steadily declined, attaining a minimum of 3.7 K/W at the highest applied power of  $\sim 28.7$  W. It should be noted that acetone more readily wets the PHP casing material compared to water, which may also contribute to its improved performance.

#### 4.6. Flow visualization in center-heating and end-heating modes

Understanding the flow behavior is essential for optimizing the heat transfer process in PHPs. Prior investigations have shown that PHPs initially exhibit oscillatory flow upon startup, which gradually transitions into pulsating and eventually circulating flow as heat flux increases [40–42]. In this visualization study, flow behavior was analyzed for 10T-C and 10T-E, under varying input power in both horizontal and vertical orientations, with acetone as the working fluid mixed with a small amount of A-22 isopropyl alcohol-based dye. The inclusion of dye is thought to have minimal effect on the working fluid thermophysical properties due to the small amount and the lower vapor pressure of isopropyl alcohol relative to acetone. To facilitate visualization of all

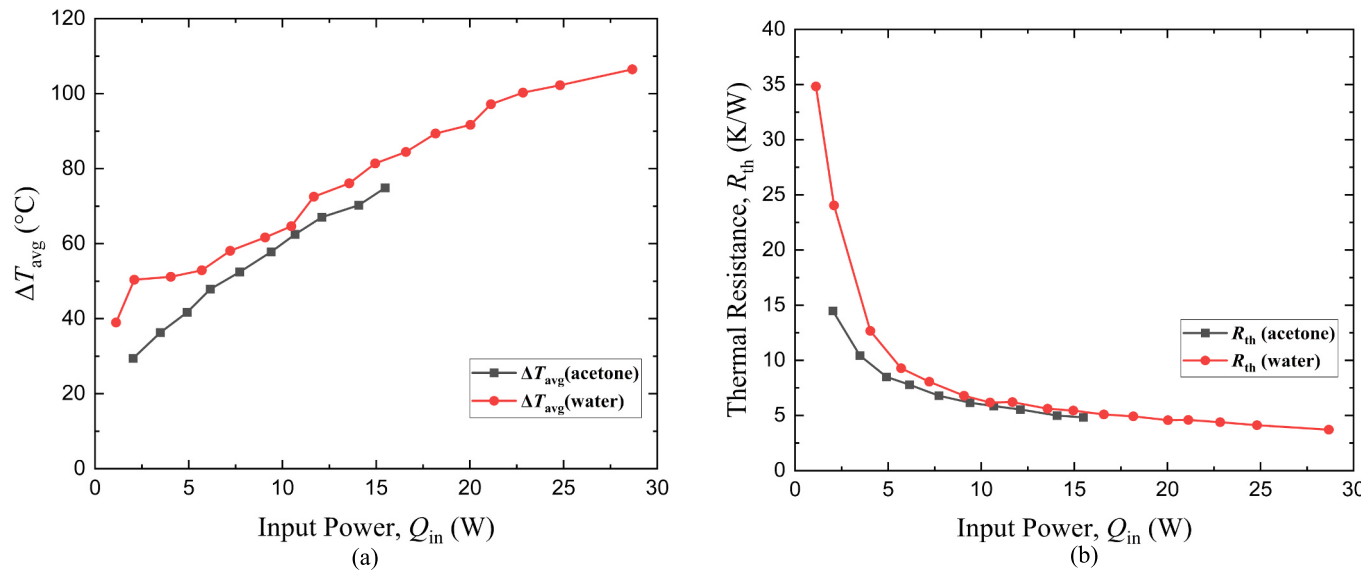


Fig. 9. Thermal performance comparison: (a)  $\Delta T_{\text{avg}}$  and (b)  $R_{\text{th}}$  for acetone and DI water.

zones—evaporator, condenser, and adiabatic—a transparent polycarbonate panel was installed on one side, leaving it less insulated than in other experiments. Consequently, instead of the two-heater, four-condenser configuration, a single heater, and two condensers were positioned on the opposite side with insulation.

The observed flow behaviors are classified in Table 3, where LO, IO, and SO denote Local Oscillation, Intermittent Oscillation, and Stable Oscillation, respectively. LO describes oscillations restricted to a few channels while the liquid in other channels remains stagnant. IO occurs when liquid oscillation amplitudes change over time cyclically, which may include brief periods of flow stagnation. SO is defined by a steady, repeating oscillatory pattern. In the current study, PHPs operating with SO featured small oscillation amplitudes between 1 and 10 mm. While IO operation includes a range of oscillation amplitudes, including occasional larger oscillations and liquid slug movements. Here, a large oscillation is defined as reaching half the channel length in amplitude.

This visualization study considered a terminal temperature of 100 °C, with no detectable flow motion below 8 W in any configuration. The 10T-E horizontal configuration demonstrated the highest heat input ( $Q_{\text{elc}}$ ), reaching 17.5 W, where all three types of flow oscillations (LO, IO, and SO) were distinctly identified. The corresponding thermal resistance plot is shown in Fig. 10 for all observed configurations. Across all cases,  $R_{\text{elc}}$  generally decreases with increasing input power,  $Q_{\text{elc}}$ . Both horizontal orientations (10T-E and 10T-C) started up well, whereas the vertical configurations failed to initiate small oscillations. Notably, the center-vertical orientation exhibited significantly higher thermal resistance and operated over a narrower power range. These findings are further illustrated and discussed in Figs. 11–13.

Fig. 11 illustrates the flow behavior of the 10T-E horizontal PHP under different heat inputs. At a lower power of approximately 10 W, nucleate boiling and LO occurred in two channels, while the others remained passive, showing no liquid-vapor phase change, as indicated by the dashed rectangular box in Fig. 11(a). These passive channels exhibit stagnant fluid behavior, suggesting that heat input was not yet

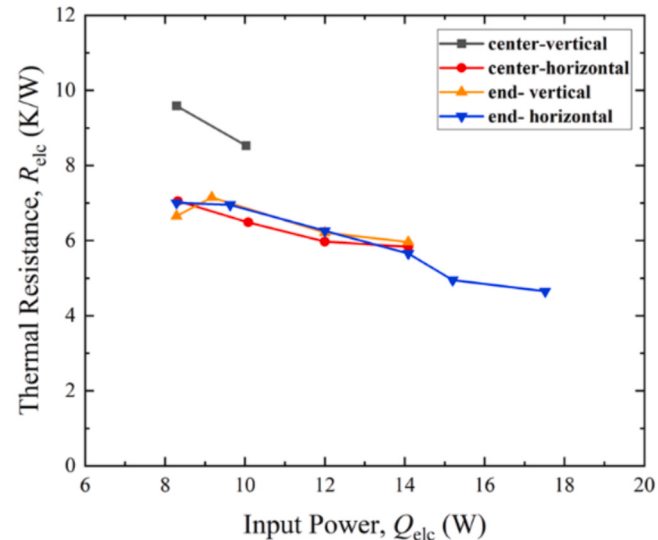


Fig. 10. Variation of thermal resistance with input power in visualization study.

sufficient to initiate oscillations throughout the structure. Raising the heat input to 12 W resulted in IO that included occasional large amplitude movements of liquid, smaller scale oscillations, and periods without liquid motion. This behavior reflects a transitional regime before stable oscillations.

At 14 W, stable oscillations (SO) were observed. This transition is correlated with an improvement in performance, as shown in Fig. 10, where thermal resistance experiences a significant drop after when the heat load is increased beyond 14 W. Nucleate boiling is not visible at 14 or 15 W, suggesting vaporization is occurring through thin film evaporation. At 17.5 W, a sequence of consecutive bubbles was observed in some channels, as shown in Fig. 11(d). A similar observation was reported by Candere et al. [1]. This phenomenon may occur due to localized and temporary nucleate boiling, or due to the breakup of larger liquid slugs into smaller segments, driven by higher inertial forces as liquid slugs navigate a turn in the PHP channel. It should be noted that even at 17.5 W nucleate boiling is not consistently observed, indicating that thin film evaporation is responsible for a majority of the

Table 3  
Flow visualization for different configurations of PHP.

Configurations	8 W	10 W	12 W	14 W	15 W	17.5 W
a) 10T-E horizontal	—	LO	IO	SO	SO	SO
b) 10T-E vertical	—	LO	LO	LO	N/A	N/A
c) 10T-C horizontal	SO	SO	SO	IO	N/A	N/A
d) 10T-C vertical	IO	IO	N/A	N/A	N/A	N/A

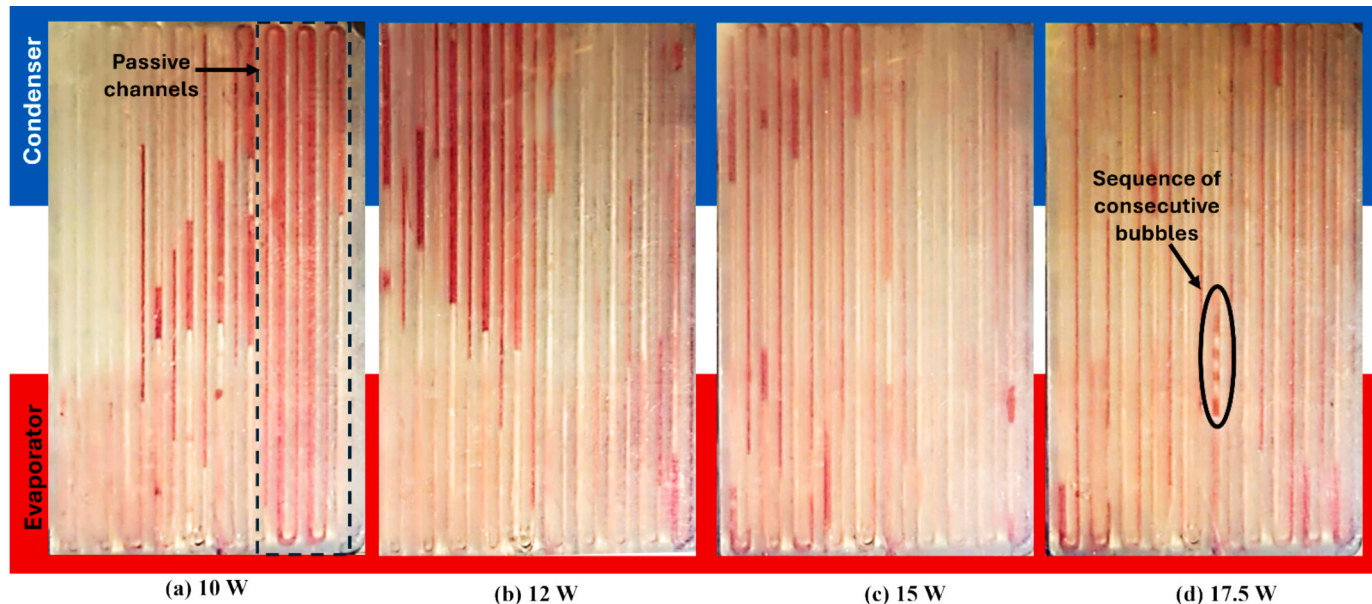


Fig. 11. Flow behavior of 10T-E horizontal PHP at different power inputs.

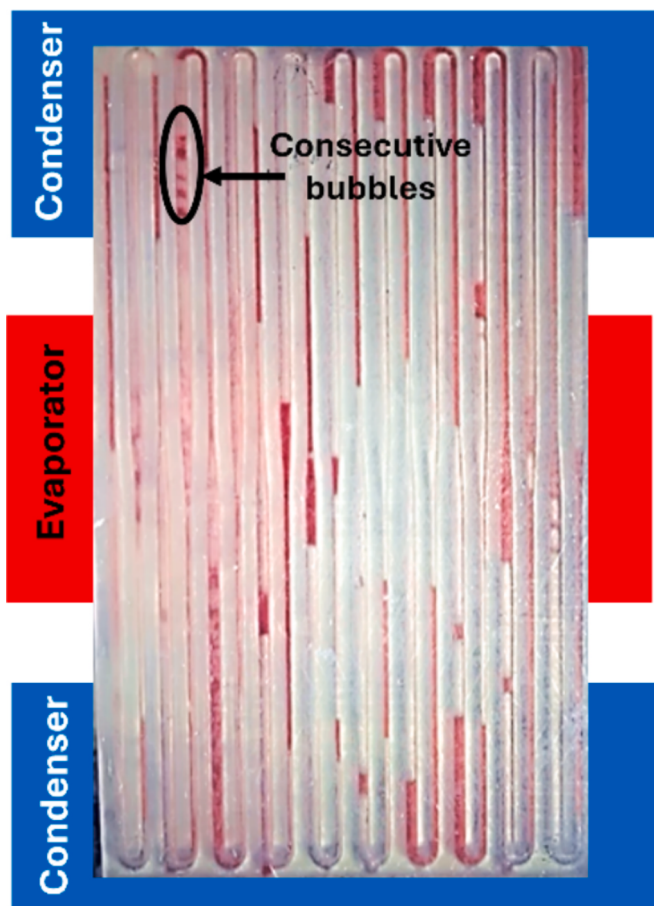


Fig. 12. Flow behavior of 10T-C horizontal PHP at 14 W.

evaporation that occurs.

The 10T-C horizontal configuration presents some differences in flow behavior from the 10T-E horizontal configuration. SO appeared at a lower heat input of 8 W. At 14 W IO occurred which consisted of steady periods of oscillations on the order of 10 s followed by shorter periods of

large oscillations and flow stagnation. This IO is likely responsible for the increased temperature drop of 10T-C compared to 10T-E in the horizontal configuration. A series of consecutive bubbles also appeared at its highest power input of 14 W, as depicted in Fig. 12, resembling the behavior observed in the 10T-E horizontal case. The corresponding resistance plot for the 10T-C case, as shown in Fig. 10, closely follows the resistance values of the 10T-E horizontal configuration across comparable heat input ranges up to 14 W. However, the 10T-E experienced a significant reduction in resistance after 14 W, while 10T-C could not be run past 14 W because the evaporator temperature limitation was reached. In both horizontal configurations, neither stable large oscillations nor circulation were observed. The lack of stable large oscillations is likely due to the low heat transport through the PHP channels which reduces the rate of vaporization and condensation and prevents large oscillations [37]. Circulation typically occurs due to buoyancy forces, which are absent in the horizontal orientation. Circulation could also occur due to the capillary forces between the dual-diameter channels; however, the large temperature drop present in these experiments likely leads to large pressure differences in the PHP which prevent the dominance of capillary pressure differences that would be required to drive circulating flow.

SO was not achieved in either of the vertical configurations across the tested range, though occasional isolated and intermittent small oscillations were observed. The 10T-C vertical case reached a maximum heat input of 10 W, whereas the 10T-E vertical configuration only went up to 14 W. Part of this behavior can be attributed to the liquid distribution, as illustrated in Fig. 13. For the 10T-C vertical setup, gravitational effects caused most of the liquid to pool at the bottom after a short time of heating, as depicted in Fig. 13(a). In the 10T-C case, IO was observed that featured occasional rapid oscillations that were very small. It appears gravitational effects acted to dampen oscillations of liquid slugs near the bottom of the channel. During the 10T-E vertical case, only localized oscillations were observed; however, the performance was superior to that of the 10T-C vertical case. This is likely a result of a more effective thermosyphon-like operation in 10T-E, in which evaporation occurs in the heated section and the hot vapor rises to the top where it is condensed in the cooled section and falls back to the evaporator through falling films. Cheng and Wong [43] also observed the thermosyphon effect before startup in their visualization study of a vertically oriented glass PHP, further supporting this hypothesis. The thermosyphon-like operation is less effective in 10T-C because the

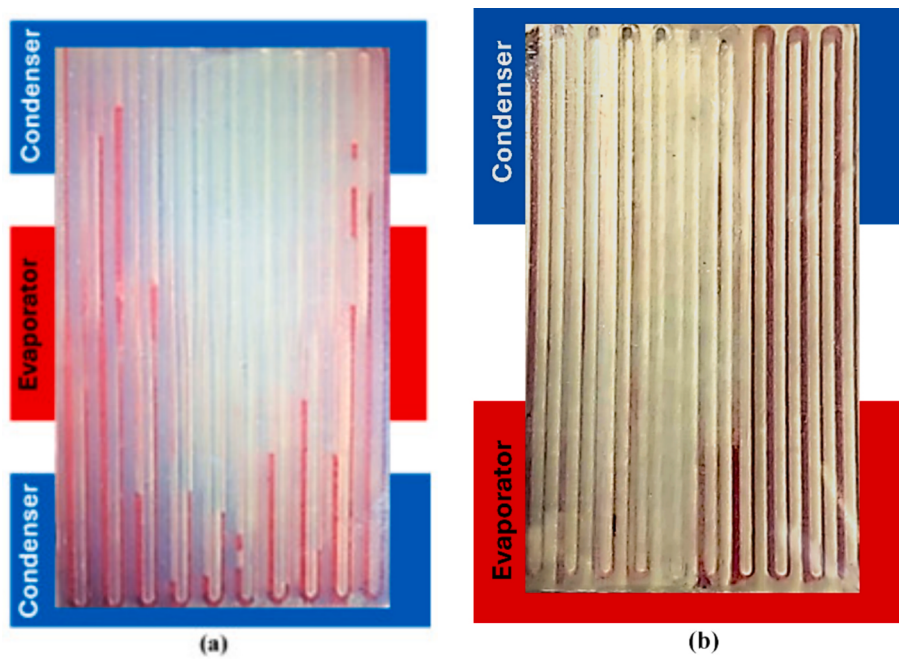


Fig. 13. Observed fluid distribution in (a) 10T-C and (b) 10T-E vertical PHPs.

evaporator is not located at the bottom of the system, and only one of the condensers is located at the top.

In the 10T-E vertical orientation, most of the liquid accumulated in 7 channels on the right side, with no vapor plugs forming within these turns, as depicted in Fig. 13(b). The effective thermosyphon-like operation combined with the low heat flux likely prevents bubble generation that could act to redistribute the liquid.

These findings suggest that the initial distribution of the working fluid considerably influences startup behavior at vertical orientation, particularly at lower heat inputs. Further investigation and experimentation are necessary to precisely understand this impact, which extends beyond the scope of the current study. Circulation was not observed in either of these cases despite the vertical orientation. The absence of liquid motion likely allows gravity to dominate, preventing the necessary flow to elevated condenser regions. This, in turn, inhibits the Rayleigh-Taylor instability and the initiation of circulation [44].

#### 4.7. Effective thermal conductivity

Reporting the effective conductivity of polymer PHPs is important because it can be easily compared to solid materials for thermal management applications. Typically, the effective thermal conductivity of any heat pipe is calculated by modeling the heat pipe as a solid material of constant conductivity and applying Fourier's law, where the length from the center of the evaporator section to the center of the condenser section  $l_{e-c}$  is the relevant length. For the 10T-E,

$$k_{\text{PHP}} = \frac{Q_{\text{in}} l_{e-c}}{\Delta T_{\text{ave}} A_c} \quad (20)$$

In the case of 2T-C and 10T-C, heat travels in two separate directions, therefore the geometry is split down the center line and the effective thermal conductivity is given by

$$k_{\text{PHP}} = \frac{0.5 Q_{\text{in}} l_{e-c}}{\Delta T_{\text{ave}} A_c} \quad (21)$$

Typically, heat pipes have higher effective thermal conductivities than any solid material they are attached to, including any heat source or heat sink attached to the device. However, polymer heat pipes have lower effective thermal conductivities due to the low thermal

conductivity of the casing material, and therefore heat sources and heat sinks made of metal may have significant capacity for conduction relative to the heat pipe. In that case, Eqs. (20) and (21) yield an effective conductivity value that is artificially higher than the true value, because the heat sources and heat sinks act to substantially reduce the axial temperature gradients in the evaporator and condenser of the heat pipe.

A more conservative approach to approximating effective thermal conductivity is to utilize the equations in section 3.3. Since  $h^*$  is known from the uncharged experiments for heat PHP design,  $k_{\text{php}}$  can be substituted for  $k_r$  and the system of equations can be solved for any PHP data point collected to determine  $k_{\text{php}}$ . This will lower the effective conductivity for two reasons: the analysis is now assuming the PHP transport length is only the length of the adiabatic section, while the lengths of the evaporator and condenser sections are ignored, and the analysis also includes the heat lost from the adiabatic section (which is not completely adiabatic) to the environment, which reduces the heat load of the PHP.

To explore the effective conductivity of the PHPs in the current work, the effective conductivities were calculated at the maximum heat transport value for each unique case, using both methods described in this section. In all of these cases, the point of maximum heat transport corresponded to the point of maximum effective thermal conductivity.

The results in Table 4 demonstrate a significant difference, sometimes larger than an order of magnitude, between the methods used to calculate effective thermal conductivity. The best representation of the effective thermal conductivity is bounded by these two values, however, it is likely closer to the more conservative approach. The discrepancy is particularly significant in 10T-E because the long, single adiabatic

Table 4  
Comparison of effective thermal conductivity.

Configurations	k-conventional Eqs. (20) and (21), W/m·K	k-conservative Eqs. (3)–(5), W/m·K
2T-C vertical	28.35	2.43
10T-C vertical	8.55	1.28
10T-C horizontal	7.23	1.06
10T-E vertical	30.01	1.28
10T-E horizontal	25.88	0.76
10T-E vertical (water)	39.08	4.77

section which must transport the entire heat load gives off significant heat to the environment. 2T-C has a higher effective conductivity than 10T-C in all cases because of its reduced evaporator length, in addition to its generally superior performance, as discussed in section 4.3.

Candere et al. [1] reported that their PHP reached a maximum effective thermal conductivity of 332.2 W/m K, which is almost 10 times larger than the maximum effective thermal conductivity reported in the present work. From the description of their experiment, it appears the discrepancy is primarily due to the neglect of losses in their analysis, which assumed the entire electrical power supplied was transported through the PHP. The losses are thought to be particularly high in their experiment due to the direct contact of one of the evaporator sides with an uninsulated aluminum plate used to hold the PHP in place. This aluminum plate likely acted as a heat sink and removed a significant portion of the heat load.

This analysis demonstrates the difficulty involved when evaluating the effective conductivity of heat pipes made of low-conductivity materials such as polymers. When evaluating polymer heat pipes for applications, it is clearly critical to account for the conduction capacity of attached heat sources and sinks, as well as heat transfer to the ambient. This can be accomplished through the conservative effective conductivity analysis demonstrated here, or by experimentation in an environment directly representative of the application that uses a solid material of moderate conductivity as a control.

#### 4.8. Uncertainty in thermal performance assessment

Fig. 14 shows examples of the relative scale of uncertainty in the context of comparing PHP performance. Fig. 14(a) presents the uncertainty in  $\Delta T_{\text{avg}}$  and  $Q_{\text{in}}$  for 10T-C and 10T-E with respect to input power. The uncertainty in input power gradually rises with increasing heat input in both cases, becoming more pronounced at higher heat levels. Meanwhile, the uncertainty in  $\Delta T_{\text{avg}}$  remains relatively stable across both configurations. This suggests that while the power uncertainties are heat-dependent, the thermal resistance behavior remains robust within the measurement sensitivity. Both configurations exhibit overlapping uncertainty ranges at moderate and high power inputs.

Fig. 14(b) illustrates the uncertainty analysis for  $R_{\text{th}}$  and  $Q_{\text{in}}$ . The uncertainty of  $R_{\text{th}}$  diminishes rapidly with an increase in  $Q_{\text{in}}$ , while the uncertainty of  $Q_{\text{in}}$  increases linearly, which again leads to overlapping uncertainty ranges at moderate and high power outputs. At higher heating levels, the distinction in thermal performance relative to low

and moderate heating levels becomes more credible despite larger uncertainties in input power. It can be observed that the performance difference between 3.8 W and 6.5 W of heating is significant relative to the experimental uncertainty.

## 5. Conclusions

The present study investigated the thermal performance and flow behavior of SLA-manufactured PHPs with dual-diameter channels. Three different configurations of PHP were tested in both horizontal and vertical orientations, along with an uncharged test for baseline comparison. Acetone was used as the working fluid in all cases except one, where deionized water was tested to compare the thermal performance of PHPs at temperatures  $>100$  °C. The analyses provide detailed insights into performance optimization and highlight challenges associated with polymer-based heat pipes. The results emphasize the significance of channel geometry alongside manufacturing accuracy, orientation dependence, and heating configurations, as well as effective conductivity modeling in PHP performance assessment. From the preceding discussions, the following key conclusions can be drawn.

- In the horizontal orientation, 2T-C failed to start up due to the absence of gravity, while 10T-C operated successfully. This suggests that a minimum number of turns is essential for initiating and sustaining oscillation in horizontal orientations, even with dual-diameter channels.
- Orientation-independent performance was demonstrated in 10T-C, which has a novel dual-diameter channel and center-heated channel design. To the authors' knowledge, this is the first polymer PHP to demonstrate orientation-independent performance.
- The PHP operated effectively at evaporator temperatures reaching around 121 °C. To the best of the authors' knowledge, this is the highest operating temperature reported for a polymer PHP to date.
- Flow visualization was conducted to capture the fluid movements throughout the entirety of the PHP channels. The flow stability, amplitude of oscillations, and distribution of liquid varied throughout the experiments, and the reasons for this are discussed in the context of the relevant PHP literature.
- The additive manufacturing process produced parts with significant dimensional discrepancies from the CAD files used. This made it difficult to optimize the wall thickness of the device, which is likely the most significant limitation of performance.

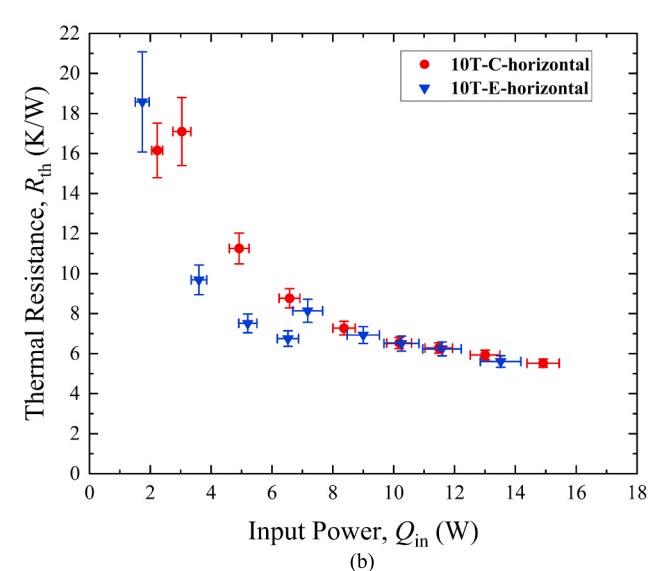
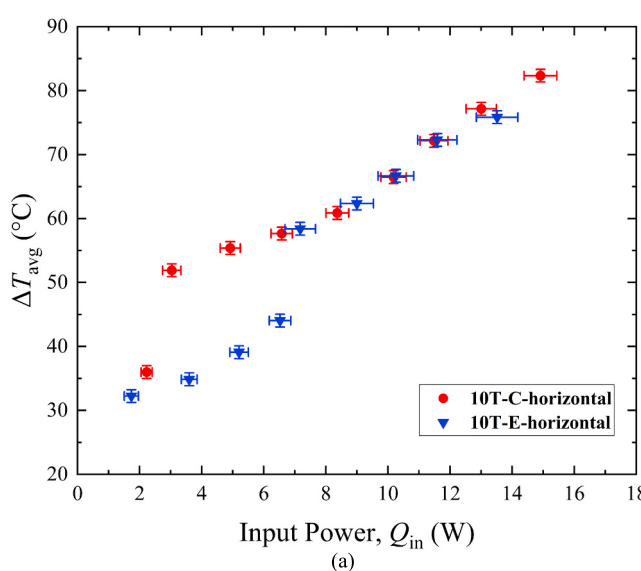


Fig. 14. Uncertainty analysis of (a)  $\Delta T_{\text{avg}}$  and (b) thermal resistance for 10T-C and 10T-E under horizontal orientation.

- Analysis of effective thermal conductivity demonstrates that the traditional approach overestimates effective thermal conductivity and is insufficient for determining the polymer PHP application space, due to the significance of axial conduction through attached heat sources and sinks. A more rigorous approach is provided to improve effective conductivity calculations.

## Declaration of Generative AI and AI-assisted technologies in the writing process

During the preparation of this work, the authors used ChatGPT to enhance the readability and language of the manuscript. Following its use, the authors reviewed and edited the content as needed and take full responsibility for the content of the published article.

## CRediT authorship contribution statement

**Md. Jubayer Hossain:** Writing – original draft, Methodology, Investigation, Formal analysis. **Max Pawlick:** Writing – review & editing, Writing – original draft, Supervision, Methodology, Formal analysis, Conceptualization. **Bhavin Yardi:** Writing – original draft, Investigation. **Satish Kumar:** Writing – review & editing, Supervision, Funding acquisition, Conceptualization.

## Declaration of competing interest

The authors declare that they have no known competing financial interests or personal relationships that could have appeared to influence the work reported in this paper.

## Acknowledgment

The authors acknowledge support from NSF Project Number CBET-2430453, United States.

## Data availability

Data will be made available on request.

## References

- [1] A. Candan Candere, et al., A novel fabrication method for polymeric flat plate pulsating heat pipe via additive manufacturing, *Appl. Therm. Eng.* 241 (September) (2024) 2023, <https://doi.org/10.1016/j.aplthermaleng.2024.122398>.
- [2] C.Y. Tseng, K.S. Yang, K.H. Chien, M.S. Jeng, C.C. Wang, Investigation of the performance of pulsating heat pipe subject to uniform/alternating tube diameters, *Exp. Therm. Fluid Sci.* 54 (2014) 85–92, <https://doi.org/10.1016/j.exthermflusci.2014.01.019>.
- [3] V.M. Patel, H.B. Mehta, Channel wise displacement-velocity-frequency analysis in acetone charged multi-turn Closed Loop Pulsating Heat Pipe, *Energy Convers. Manag.* 195 (May) (2019) 367–383, <https://doi.org/10.1016/j.enconman.2019.05.014>.
- [4] H. Akachi, Structure of a Heat Pipe, 1990 [Online]. Available: <https://patentimages.storage.googleapis.com/db/4d/08/b2e8835cf995b9/US4921041.pdf>.
- [5] H. Akachi, Structure of micro-heat pipe, 1993 [Online]. Available: <https://patentimages.storage.googleapis.com/8d/87/57/18fa8dfa9abc67/US5219020.pdf>.
- [6] V. Patel, Gaurav, H. Mehta, Influence of working fluids on startup mechanism and thermal performance of a closed loop pulsating heat pipe, *Appl. Therm. Eng.* 110 (2016) 1568–1577, <https://doi.org/10.1016/j.aplthermaleng.2016.09.017>.
- [7] Y. Ji, H.H. Chen, Y.J. Kim, Q. Yu, X. Ma, H.B. Ma, Hydrophobic surface effect on heat transfer performance in an oscillating heat pipe, *J. Heat Transfer* 134 (7) (2012) 1–3, <https://doi.org/10.1115/1.4006111>.
- [8] P. Charoensawan, S. Khandekar, M. Groll, P. Terdtoon, Closed loop pulsating heat pipes: Part A: parametric experimental investigations, *Appl. Therm. Eng.* 23 (16) (2003) 2009–2020, [https://doi.org/10.1016/S1359-4311\(03\)00159-5](https://doi.org/10.1016/S1359-4311(03)00159-5).
- [9] D. Bastakoti, H. Zhang, D. Li, W. Cai, F. Li, An overview on the developing trend of pulsating heat pipe and its performance, *Appl. Therm. Eng.* 141 (2018) 305–332, <https://doi.org/10.1016/j.aplthermaleng.2018.05.121>.
- [10] M. Alhuyi Nazari, M.H. Ahmadi, R. Ghasempour, M.B. Shafii, How to improve the thermal performance of pulsating heat pipes: a review on working fluid, *Renew. Sustain. Energy Rev.* 91 (April) (2018) 630–638, <https://doi.org/10.1016/j.rser.2018.04.042>.
- [11] S. Okazaki, H. Fukie, H. Ogawa, Performance of circular Oscillating Heat Pipe for highly adaptable heat transfer layout, *Appl. Therm. Eng.* 198 (August) (2021) 117497, <https://doi.org/10.1016/j.aplthermaleng.2021.117497>.
- [12] M.B. Shafii, A. Faghri, Y. Zhang, Thermal modeling of unlooped and looped pulsating heat pipes, *J. Heat Transfer* 123 (6) (2001) 1159–1172, <https://doi.org/10.1115/1.1409266>.
- [13] S. Rittidech, N. Pipatpaiboon, P. Terdtoon, Heat-transfer characteristics of a closed-loop oscillating heat-pipe with check valves, *Appl. Energy* 84 (5) (2007) 565–577, <https://doi.org/10.1016/j.apenergy.2006.09.010>.
- [14] C.Y. Tseng, K.S. Yang, C.C. Wang, Non-uniform three-dimensional pulsating heat pipe for anti-gravity high-flux applications, *Energies* 13 (12) (2020) 1–16, <https://doi.org/10.3390/en13123068>.
- [15] G.H. Kwon, S.J. Kim, Experimental investigation on the thermal performance of a micro pulsating heat pipe with a dual-diameter channel, *Int. J. Heat Mass Transf.* 89 (2015) 817–828, <https://doi.org/10.1016/j.ijheatmasstransfer.2015.05.091>.
- [16] M.J. Hossain, M. Pawlick, V.T. Le, A. Tikadar, X. Zhang, S. Kumar, Investigation of flow and thermal performance in a non-uniform channel pulsating heat pipe additively manufactured from high-temperature resin, *Intersoc. Conf. Therm. Thermomechanical Phenom. Electron. Syst. IITHERM* (2024) 1–7, <https://doi.org/10.1109/IITHERM5375.2024.10709549>.
- [17] S.D. Nath, S. Nilur, An overview of additive manufacturing of polymers and associated composites, *Polymers (Basel)* 12 (11) (2020) 1–33, <https://doi.org/10.3390/polym12112719>.
- [18] H. Rastan, A. Abdi, B. Hamawandi, M. Ignatowicz, J.P. Meyer, B. Palm, Heat transfer study of enhanced additively manufactured minichannel heat exchangers, *Int. J. Heat Mass Transf.* 161 (2020), <https://doi.org/10.1016/j.ijheatmasstransfer.2020.120271>.
- [19] D. Jafari, W.W. Wits, B.J. Geurts, Metal 3D-printed wick structures for heat pipe application: capillary performance analysis, *Appl. Therm. Eng.* 143 (May) (2018) 403–414, <https://doi.org/10.1016/j.aplthermaleng.2018.07.111>.
- [20] K.L. Chen, K.Y. Luo, P.P. Gupta, S.W. Kang, SLM additive manufacturing of oscillating heat pipe, *Sustain.* 15 (9) (2023), <https://doi.org/10.3390/su15097538>.
- [21] T. Arai, M. Kawaji, Thermal performance and flow characteristics in additive manufactured polycarbonate pulsating heat pipes with Novec 7000, *Appl. Therm. Eng.* 197 (January) (2021) 117273, <https://doi.org/10.1016/j.aplthermaleng.2021.117273>.
- [22] O.T. Ibrahim, et al., An investigation of a multi-layered oscillating heat pipe additively manufactured from Ti-6Al-4V powder, *Int. J. Heat Mass Transf.* 108 (2017) 1036–1047, <https://doi.org/10.1016/j.ijheatmasstransfer.2016.12.063>.
- [23] Y. Koito, M. Kawaji, Performance of a pulsating heat pipe fabricated with a 3-D printer, *ASME 2017 Heat Transf Summer Conf. HT* 2 (2017) 2017, <https://doi.org/10.1115/HT2017-4816>.
- [24] Y. Koito, F. Hideyama, Heat transfer characteristics of an ABS polymer pulsating heat pipe fabricated by a 3-D printer, *Therm. Sci. Eng.* 27 (2) (2019) 59–66.
- [25] Y. Koito, H. Yoshida, Z. Pei, An experimental study of a polymer pulsating heat pipe 3D-printed on a thin polymer sheet, *Multiph. Sci. Technol.* 33 (4) (2021) 31–43, <https://doi.org/10.1615/MultSciTechn.2021040052>.
- [26] K.H. Chien, Y.T. Lin, Y.R. Chen, K.S. Yang, C.C. Wang, A novel design of pulsating heat pipe with fewer turns applicable to all orientations, *Int. J. Heat Mass Transf.* 55 (21–22) (2012) 5722–5728, <https://doi.org/10.1016/j.ijheatmasstransfer.2012.05.068>.
- [27] K. Luo, A.J. Gross, J. Brown, W. Chang, C. Li, A fully 3D-printed flexible polymeric heat pipe, *J. Therm. Sci. Eng.* 16 (9) (2024) 1–8, <https://doi.org/10.1115/1.4065748>.
- [28] X. Chen, X. Liu, D. Xu, Y. Chen, Thermal performance of a tandem-dual-channel flat-plate pulsating heat pipe applicable to hypergravity, *Int. J. Heat Mass Transf.* 189 (2022) 122656, <https://doi.org/10.1016/j.ijheatmasstransfer.2022.122656>.
- [29] M. Pagac, et al., A review of vat photopolymerization technology: Materials, applications, challenges, and future trends of 3d printing, *Polymers (Basel)* 13 (4) (2021) 1–20, <https://doi.org/10.3390/polym13040598>.
- [30] G. Nellis, S. Klein, *Heat Transfer*, Cambridge University Press, 2008.
- [31] L. Kossel, J. Pfotenhauer, F. Miller, Development of a novel orientation-independent hybrid conventional-pulsating heat pipe using cryogenic helium, *Int. J. Heat Mass Transf.* 237 (November) (2024), <https://doi.org/10.1016/j.ijheatmasstransfer.2024.126430>.
- [32] E. Universit, C. Mai, P.H. Pipes, C. Loop, O. Loop, Closed and Open Loop Pulsating Heat Pipes, vol. 26, 2004.
- [33] H. Yang, S. Khandekar, M. Groll, Operational limit of closed loop pulsating heat pipes, *Appl. Therm. Eng.* 28 (1) (2008) 49–59, <https://doi.org/10.1016/j.aplthermaleng.2007.01.033>.
- [34] B.L. Drolen, C.D. Smoot, Performance limits of oscillating heat pipes: theory and validation, *J. Thermophys. Heat Transf.* 31 (4) (2017) 920–936, <https://doi.org/10.2514/1.TS105>.
- [35] A. Yoon, S.J. Kim, Characteristics of oscillating flow in a micro pulsating heat pipe: fundamental-mode oscillation, *Int. J. Heat Mass Transf.* 109 (2017) 242–253, <https://doi.org/10.1016/j.ijheatmasstransfer.2017.02.003>.
- [36] J. Lee, Y. Joo, S.J. Kim, Effects of the number of turns and the inclination angle on the operating limit of micro pulsating heat pipes, *Int. J. Heat Mass Transf.* 124 (2018) 1172–1180, <https://doi.org/10.1016/j.ijheatmasstransfer.2018.04.054>.
- [37] M. Pawlick, An Analytical Model for Oscillating Heat Pipe Performance and Experimental Testing of a Novel Helix-Shaped Design, Georgia Institute of Technology, 2024. [Online]. Available: <https://hdl.handle.net/1853/75740>.
- [38] Y. Ji, C. Chang, G. Li, H. Ma, An Investigation on Operating Limit of an Oscillating Heat Pipe, 2014. doi: [10.1615/IHTC15.hpp.009442](https://doi.org/10.1615/IHTC15.hpp.009442).

- [39] D. Zhang, Z. He, E. Jiang, C. Shen, J. Zhou, A review on start-up characteristics of the pulsating heat pipe, *Heat Mass Transf. Und Stoffuebertragung* 57 (5) (2021) 723–735, <https://doi.org/10.1007/s00231-020-02998-4>.
- [40] J. Kim, S.J. Kim, Experimental investigation on working fluid selection in a micro pulsating heat pipe, *Energy Convers. Manag.* 205 (October 2019) (2020), <https://doi.org/10.1016/j.enconman.2019.112462>.
- [41] J. Qu, H. Wu, P. Cheng, Start-up, heat transfer and flow characteristics of silicon-based micro pulsating heat pipes, *Int. J. Heat Mass Transf.* 55 (21–22) (2012) 6109–6120, <https://doi.org/10.1016/j.ijheatmasstransfer.2012.06.024>.
- [42] H. Yang, S. Khandekar, M. Groll, Performance characteristics of pulsating heat pipes as integral thermal spreaders, *Int. J. Therm. Sci.* 48 (4) (2009) 815–824, <https://doi.org/10.1016/j.ijthermalsci.2008.05.017>.
- [43] P.S. Cheng, S.C. Wong, Detailed visualization experiments on the start-up process and stable operation of pulsating heat pipes: effects of internal diameter, *Int. J. Heat Fluid Flow* 106 (January) (2024) 109325, <https://doi.org/10.1016/j.ijheatfluidflow.2024.109325>.
- [44] M. Pawlick, G.P. Peterson, An analytical model of oscillating heat pipe performance, *Therm. Sci. Eng. Prog.* 50 (March) (2024) 102517, <https://doi.org/10.1016/j.tsep.2024.102517>.